Journal of Applied Fluid Mechanics, Vol. 17, No. 4, pp. 742-755, 2024.
Available online at www.jafmonline.net, ISSN 1735-3572, EISSN 1735-3645.
https://doi.org/10.47176/jafm.17.4.2276

Applying Machine Learning in CFD to Study the Impact of Thermal Characteristics on the Aerodynamic Characteristics of an Airfoil

A. Wadi Al-Fatlawi [1, 2†], J. Hashemi [2], S. Hossain [3, 4] and M. El Haj Assad [5]

[1]*Department of Mechanical Engineering, University of Kufa, Najaf, Iraq*
[2]*Department of Mechanical Engineering, Ferdowsi University of Mashhad, Mashhad, Iran*
[3] *Institute for Energy Research, Jiangsu University, Zhenjiang, 212013, P.R. China*
[4] *School of the Environment and Safety Engineering, Institute for Energy Research, Jiangsu University, Zhenjiang, 212013, P.R. China*
[5]*Department of Sustainable and Renewable Energy Engineering, University of Sharjah, Sharjah 27272, United Arab Emirates*

†Corresponding Author Email: aliw.alfatlawi@uokufa.edu.iq

ABSTRACT

A computational fluid dynamic (CFD) and machine learning approach is used to investigate heat transfer on NASA airfoils of type NACA 0012. Several different models have been developed to examine the effect of laminar flow, Spalart flow, and Allmaras flow on the NACA 0012 airfoil under varying aerodynamic conditions. Temperature conditions at high and low temperatures are discussed in this article for different airfoil modes, which are porous mode and non-porous mode. Specific parameters included permeability of 11.36 x 10-10 m^2, porosity of 0.64, an inertia coefficient of 0.37, and a temperature range between 200 K and 400 K. The study revealed that a temperature increase can significantly increase lift-to-drag. Additionally, employing both a porous state and temperature differentials further contributes to enhancing the lift-to-drag coefficient. The neural network also successfully predicted outcomes when adjusting the temperature, particularly in scenarios with a greater number of cases. Nevertheless, this study assessed the accuracy of the system using a SMOTER model. It has been shown that the MSE, MAE, and R for the best performance validation of the testing case were 0.000314, 0.0008, and 0.998960, respectively, at K = 3. However, the study shows that epoch values greater than 2000 increase computational time and cost without improving accuracy. This indicates that the SMOTER model can be used to classify the testing case accurately; however, higher epoch values are not necessary for optimal performance.

Article History

Received September 5, 2023
Revised November 5, 2023
Accepted November 28, 2023
Available online January 30, 2024

Keywords:

Computational modeling
Aerodynamics
Subsonic flow around airfoils
Heat transfer
Machine learning
CFD

1. INTRODUCTION

The aerodynamic properties of fluid flow around a wing or airfoil are usually forecasted using numerical methods, which are crucial for aerospace industry design. Machine learning techniques (MLT) for forecasting, especially in fluid dynamics, have increased in recent years, reducing both the time and cost of using numerical methods. The study of fluid flow around airfoils is an important component of fluid mechanics because it can lead to improved airfoil designs, increased aerodynamic efficiency, and improved safety and stability in a variety of engineering systems. Fluid flow behavior around airfoils provides important information about fluid-structure interaction, boundary layer separation, and vortex shedding, all of which are important aspects of hydro-aerodynamics. Flow separation occurs when the fluid flow around an airfoil detaches from the surface, leaving a wake of vortices behind it that can impair hydro-aerodynamic performance by reducing lift and increasing drag. Various design modifications, such as trailing/leading edge extensions (Llorente & Ragni, 2020; Ethiraj & Pillai, 2021; Seyhan et al., 2021; Zadorozhna et al., 2021), vortex generators (Li et al., 2019; Yan et al., 2019; Silva & Malatesta, 2020), and blowing/suction systems (Fahland et al., 2021; Chen et al., 2022; Wang et al., 2022), are utilized to maintain attached fluid flow over a greater portion of the airfoil's surface.

Several different studies, such as (Mabey, 1990;Hinz et al., 2013; Samiee et al., 2018; Jordaan et al., 2021; Liu et al., 2023) suggest that heat transfer can have complex effects on the flow separation and aerodynamic performance of airfoils in subsonic flows, and the outcome depends on a variety of factors, including the speed,

NOMENCLATURE

a	speed of sound, a = √kRT	p	pressure
c	airfoil chord length	P_r	Prandtl number, Pr = μC$_P$/k$_T$
C_F	inertia coefficient	R_e	Reynolds number, Re = U$_\infty$c/ν
C_P	specific heat at constant pressure	T	temperature
C_v	specific heat at constant volume	T_∞	freestream temperature
h	specific enthalpy, h = e+p/ρ	U_∞	freestream velocity
k_T	thermal conductivity	ΔT	temperature difference between freestream and surface, ΔT = T$_h$-T$_\infty$
M_a	Mach number, Ma = U$_\infty$/a	μ	dynamic viscosity

temperature, and materials used. Heating of airfoil surfaces can lead to an increase in the thermal boundary layer thickness, where the temperature difference between the surface and the freestream causes spurious scale effects and hastens flow separation (Norton et al., 1973). Heat transfer can also change the pressure distribution on the airfoil surface, altering the flow separation and reattachment points. This separation can result in increased drag, decreased lift, and reduced stability (Landrum & Macha, 1987). Heating the airfoil surface can lead to an increase in the size of the separated region, which results in reduced aerodynamic performance (Landrum & Macha, 1987; Liepmann & Fila, 1947). Depending on the pressure gradient, heating the airfoil surface can also influence skin friction as it affects the fluid viscosity and velocity gradient near the airfoil surface (Stock, 2002). Therefore, it appears that controlling heat transfer and temperature on the surface of airfoils could be a promising strategy for enhancing the aerodynamic performance of airfoils, particularly in subsonic flow conditions (Raghunathan & Mitchell, 1995).

A variety of design strategies, such as using advanced materials with high thermal conductivity and applying cooling techniques, are utilized to maintain the airfoil surface temperature within a desired range to enhance lift, reduce drag, and increase the envelope of operation for airfoils. Kim et al. and his team (Kim et al., 2003) showed that the aerodynamic performance of small-scale airfoils can be improved by varying the airfoil surface temperature. They found that heating the lower surface and cooling the upper surface of small-scale airfoils increases lift and decreases drag. Nevertheless, they restricted their attention to symmetric airfoils, and the simulation was completed at a Re = 104. Bekka et al. (2009) found that the LRN range is more reasonable for thermal impacts. Additionally, they demonstrated how to utilize turbulence models; the findings are close to the experimental data obtained by simulating the flow around a NACA 0012 airfoil. CFD techniques and NS (Navier–Stokes) equations are used at Re = 3000 (Hinz et al., 2013); they studied how a flapping NACA 0012 airfoil's aerodynamic performance was affected by heat transfer. In their simulations, the airfoil's temperature was maintained as hot or cold on both surfaces.

Several numerical investigations have been carried out through CFD simulation and machine learning in airfoil aerodynamics (Selimefendigil & Öztop, 2021). Ahmed et al. (Ahmed et al., 2022) used an artificial neural network to predict aerodynamic coefficients. First, they numerically investigated the NACA0012 airfoil for different conditions and used the results of the numerical solution to learn the neural network. Their neural network included one hidden layer with ten neurons, and the output layer of their network also included two values of lift coefficient and drag coefficient. Bhatnagar et al. (Bhatnagar et al., 2019) proposed a convolutional neural network (CNN) to predict the flow field. First, they solved the flow around airfoil shapes with standard numerical methods. They used the results to learn the neural network and considered the velocity and pressure values of the flow field as the output values of the network. They analyzed the neural network results to predict the influence of the angle of attack, Reynolds number, and different shapes of airfoils. They concluded that the developed CNN could be used for design and optimization applications.

To get on the right track, in this research, we have used an artificial neural network to predict the lift coefficient with acceptable accuracy. However, it examines how surface temperature and heat transfer enhance the aerodynamic performance of small-scale airfoils. This is a step toward improving physical event modeling and producing a forecasting device that will direct future studies toward the most effective performance environments.

2. METHODOLOGY

Using the developed neural network for optimization and other applications is much faster and less expensive than conventional numerical methods. Samples have been randomly selected by the Latin Hyperbolic Sampling (LHS) method, and the results of the numerical solution of these samples have been used in the modeling of artificial neural networks. In this study, first we extract the parameters of the lift and drag coefficients from the airfoil with and without porous mode, which have different temperatures. Then, we predict the value of lift coefficients with the aid of machine learning.

2.1 Physical Description

According to earlier research, the aerodynamic performance of microscale rotors is magnitudes lower than that of their full-scale equivalents. Spin testing was done on inch (15.24 cm)-diameter micro-rotors with both NACA 0012 standard geometry and Eppler-61 advanced geometry airfoil sections. The greatest L/D ratio generated by the Eppler-61 airfoil for the rotor was only approximately 10 (Cl = 0.96 and Cd = 0.1 at ReD = 3.3×104). Still, the performance of the NACA 0012 airfoil

was much worse under the same test conditions, by more than 50%. These outcomes are consistent with the most recent test outcomes offered by (Oosedo et al., 2017). These performance indices are substantially lower than those of true high airfoils with an L/D ratio between 50 and 150. Due to their poor aerodynamic performance (L/D = 10) and poor quality factor (ratio of inspired to total power less than 0.5), microscale rotors cannot provide MAVs with a flying envelope. The longest flying time for battery-powered MAVs was 22 minutes (Grasmeyer & Keennon, 2001), which is just 35% of the Space Research Agency's target of 60 minutes. Therefore, it's essential to identify strategies to increase the aerodynamic efficiency of MAVs to allow effective, manageable, and sustained microscale flight. This research presents a novel approach to controlling thermal performance and airfoil surface temperature, significantly enhancing MAV aerodynamic performance. The thermal boundary-layer thickness, as compared to the airfoil chord, is significant for microscopic-level aeronautical lifting surfaces and can influence the flow area beyond the viscous boundary layer. Therefore, by chilling the upper surface and warming the lower surface of an airfoil section, it is feasible to decrease the temperature on the upper surface and raise pressure just on the lower surface of an airfoil, particularly in the vicinity of the airfoil's nose (for instance, using a thermoelectric device). As a result, there may be greater lift and circulation, less pressure drags, and more suction from around the airfoil's nose. Lower topmost temperature and pressure also result in faster flow through the airfoil's upper surface, which minimizes flow separation and delays separation.

2.2 Governing Equations

The continuity equation, Navier stock equations (NS), and energy equation in terms of enthalpy control non-isothermal two-dimensional flow fields around an airfoil. These equations need to be solved simultaneously to model the flow field accurately. This can be done using numerical methods, such as the finite volume or finite difference method. The numerical solution gives the pressure, temperature, and velocity distribution around the airfoil, which can be used to calculate lift and drag forces. These equations are given by the following equations (Ferziger et al., 2002):

$$\frac{\partial(\rho u_i)}{\partial \chi_i} = 0 \tag{1}$$

$$\frac{\partial(\rho u_j u_i)}{\partial \chi_j} = \frac{\partial(\tau_{ij})}{\partial \chi_j} - \frac{\partial \rho}{\partial \chi_i} \tag{2}$$

$$\frac{\partial(\rho u_j h)}{\partial \chi_j} = \frac{\partial}{\partial \chi_j}\left(\frac{k_T \partial h}{C_p \partial \chi_j}\right) + u_j \cdot \frac{\partial \rho}{\partial \chi_i} \tag{3}$$

where Eqs. (1) and (2) represent the x and y-coordinates, respectively, and u_i is the velocity in the i direction. k_T is the thermal conductivity and C_P is specific heat capacity, respectively. The enthalpy is defined as $h = e + p/\rho$, where e is internal energy, p is pressure, and ρ is density.

The energy equation includes the component Dp/Dt. The amount of kinetic energy that is transformed into heat via viscous dissipation is relatively small compared to the other variables in the energy equation; thus, it is ignored. The viscous component of the stress tensor τ_{ij} for a Newtonian fluid is defined as follows, under the assumption that the fluid is Newtonian:

$$\tau_{ij} = \mu\left(\frac{\partial u_i}{\partial \chi_j} + \frac{\partial u_j}{\partial \chi_i} - \frac{2}{3}\delta_{ij} di\upsilon\vec{u}\right) \tag{4}$$

Eq. (4) shows a relationship between the dynamic viscosity μ, and the velocity gradient perpendicular to the wall. δ_{ij} is the Kronecker symbol, and mu is the fluid's dynamic viscosity. Eq. (5) illustrates a simplified 1-D representation:

$$\tau = \mu \frac{\partial u}{\partial n} \tag{5}$$

It is assumed that gravitational forces are not present in the flow. However, gravitational forces may impact the flow and cause natural convection when there are enforced temperature variations between the surface and the free stream, which the model mentioned above will be unable to account for. The ideal gas equation is used to relate the thermodynamic state variables p, ρ, and T under the assumption that the fluid is an ideal gas. The thermodynamic equation of state is used to connect the specific enthalpy and temperature to the temperature, as shown in Eq. (7):

$$h = C_p T \tag{6}$$

$$p = \rho R T \tag{7}$$

where T and R stand for temperature and the particular gas constant, respectively.

Drag and lift coefficients, which are dimensionless representations of forces, are:

$$C_D = \frac{D}{1/2(A_{ref}\rho_\infty U_\infty^2} \tag{8}$$

$$C_L = \frac{L}{1/2(A_{ref}\rho_\infty U_\infty^2} \tag{9}$$

The Spalart-Allmaras model (Crivellini & D'Alessandro, 2014) is a one-equation turbulence model. Under the dimensional analysis presumptions, the eddy viscosity transport equation is created. The following is the eddy viscosity transfer equation:

$$\frac{\partial \tilde{v}}{\partial t} + \tilde{u}_j \frac{\partial \tilde{v}}{\partial t} = P + D_{IFF} + D_{ES} \tag{10}$$

where D_{ES},P and D_{IFF} are respectively destruction, production, and dissipation terms of $\tilde{v}$ expressed as:

$$P = c_{b1} \tilde{S} \tilde{V} \tag{11}$$

$$D_{IFF} = \frac{1}{\rho}\left[\frac{\partial}{\partial \chi_j}\left((\nu + \tilde{\nu})\frac{\partial \tilde{\nu}}{\partial \chi_j}\right) + c_{b2}\frac{\partial \tilde{\nu}}{\partial \chi_j}\frac{\partial \tilde{\nu}}{\partial \chi_j}\right] \tag{12}$$

$$D_{ES} = c_{\omega 1} f_{\omega} \left(\frac{\tilde{\nu}}{d}\right)^2 \quad (13)$$

To ensure that $\tilde{\nu} = kyu_{\tau}$ in the logarithmic part of the boundary layer, the damping function $f_{v1}$is defined as:

$$f_{v1} = \frac{x^3}{x^3 + c_{v1}^3} \quad (14)$$

Where $X = \frac{\tilde{\nu}}{\nu}$, however, S is modified to $\tilde{S}$ in order to maintain the correct behaviour ($\tilde{S} = u_{\tau}/ky$):

$$\tilde{S} = \sqrt{2\Omega_{ij}\Omega_{ij}}\, f_{v3} + \frac{\tilde{\nu}}{kd^2} f_{v2} \quad (15)$$

With $\Omega = 0.5\left(\frac{\partial \bar{u}_i}{\partial x_j} - \frac{\partial \bar{u}_j}{\partial x_j}\right)$, $f_{v2} = 1 - \frac{X}{X + f_{v1}}$ and $f_{v3} = 1$. The function f_{ω} introduced by (Kim et al., 2003):

$$f_{\omega}(g) = g\left(\frac{1 + c_{\omega 3}^6}{g + c_{\omega 3}^6}\right)^{1/6} \quad (16)$$

where g acts as a limiter, avoiding f_{ω} from become too high, and is expressed as: $g = rc_{\omega 2}(r^6 - r)$ with $r = \frac{\tilde{\nu}}{\tilde{S}kd^2}$. r, f_{ω} = 1. The constants of the model are :$c_{b1} = 0.1355$, $c_{b2} = 0.622$, $\sigma = 2/3$, $K = 0.41$, $c_{\omega 1} = \frac{c_{b1}}{k^2} + \frac{1 + c_{b2}}{\sigma}$, $c_{\omega 2} = 0.3$, $c_{\omega 3} = 2$ *and* c_{v1} = 7.1.

2.3 Computational Domain

We demonstrate numerical flow simulations using the NS flow solver, FLUENT. Polynomial extrapolation functions to the supplied airfoil shape are used to characterize the upper and lower surfaces of the airfoil. The length of the airfoil chord is 20 mm in Fig. 1.

The ideal gas law is used as the equation of state, specific heat is held constant, and the Sutherland law characteristics are employed. Even with the steady specific heat assumption, the model is still valid; assuming a constant specific heat, the model is correct since temperature gradients are usually minimal. The far-field circumstances mimic a mean flow of uniform airflow with a consistent pressure gradient, velocity, and freestream Mach number. The initial conditions of no penetration, no-slip, and a predetermined temperature

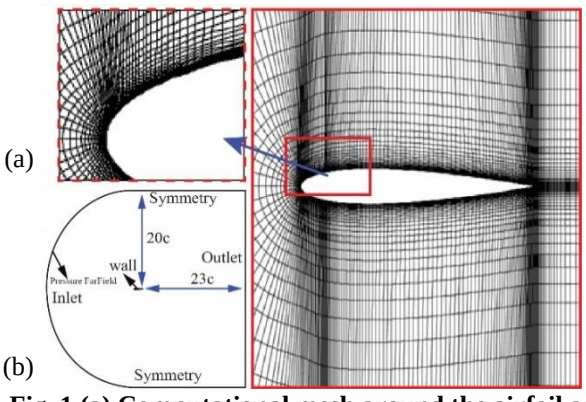

Fig. 1 (a) Computational mesh around the airfoil and (b) computational domain

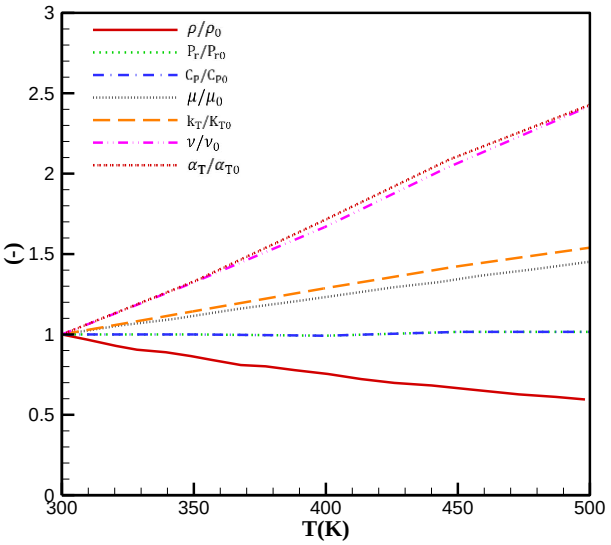

Fig. 2 Density (isobar), dynamic and kinematic viscosity dependence on temperature (Eucken, 1940; Bergman et al., 2011)

distribution are all applied to the airfoil surfaces. The relatively stable fields of velocity, warmth, density, and pressure are calculated using an implicit and iterative second-order approach that integrates the continuity, momentum, and energy equations. The modeling is done in Spalart-Allmaras turbulence mode. Moreover, about 20 airfoil chords separate the far-field (outer) control surface from the leading edge of the airfoil.

2.4 Fluid Properties

In general, fluid characteristics change as the temperature changes. A study of fluid characteristics at various temperatures is conducted to prepare for the simulations. Figure 2 demonstrates how the physical characteristics of the air change as the temperature changes (Eucken, 1940; Bergman et al., 2011). With their reference values set at 300 K, the values are then normalized. When the temperature rises, the density of the air drops, assuming an isobar change of condition. The Prandtl number (Pr=$\mu C_P/k_T$) slightly decreases, too. Over the range of temperatures being investigated, the specific heat Cp is essentially constant. The values of the dynamic viscosity m and thermal conductivity kT significantly rise as the temperature increases from 300 K to 400 K. Dynamic viscosity and kinematic viscosity are connected by $\nu = \mu/\rho$. The kinematic viscosity considerably rises in the given temperature range due to the density decreasing and the dynamic viscosity growing. The relationship between thermal conductivity k_T and thermal diffusivity α_T is given by $\alpha_T = k_T/\rho C_P$ and exhibits the same characteristics as the fluid's kinematic viscosity.

Examining air's physical characteristics leads to the conclusion that fluid properties vary significantly throughout the range of temperatures under consideration, and the simulation model must account for this. The following models and assumptions are found:

$$C_p = \text{const} = C_p(300\text{K}) = 1007\,\text{J/kgK} \quad (17)$$

$$\mu(T) = \frac{A_S \sqrt{T}}{1 + T_S / T} \tag{18}$$

$$k_T(T) = \mu(T) C_{Eucken} \tag{19}$$

Concerning the temperature range under consideration, the specific heat capacity CP exhibits a slight fluctuation. (Fig. 2) and is believed to be constant as a result. The Sutherland model is used to analyze the dynamic viscosity μ. (Eq. (18)) (Sutherland, 1893) with the parameters of A_s and T_s for air are 1.4792×10^6 kg/sm$\sqrt{K}$ and 116 K, respectively. The Sutherland model empirically correlates dynamic viscosity as a function of temperature. The correlation demonstrates excellent agreement regarding the air's tabulated qualities (Sutherland, 1893).

2.5 Machine Learning

A multilayer perceptron (MLP) neural network has been developed to predict the lift coefficient values. Due to the fact that the data related to the drag in the investigated area does not show significant changes, the focus of the neural network on the prediction of the lift coefficient and especially on the stall area has been considered. The schematic of the neural network used is given in Fig. 3. This type of neural network consists of an input layer, an output layer, and one or more hidden layers, which are the connections between the input and output layers. The values of the neurons of the input layer are transferred to the neurons of the first hidden layer after multiplying by the values of the corresponding weights. After each hidden layer, there is an activation function to cover the nonlinear conditions of the problem. Various activation functions, such as sigmoid, Tanh, and ReLU, can be used. After passing through the first hidden layer and the activation function, those values are multiplied by corresponding weights and transferred to the next hidden layer; this process continues until the numerical values are finally transferred to the output layer.

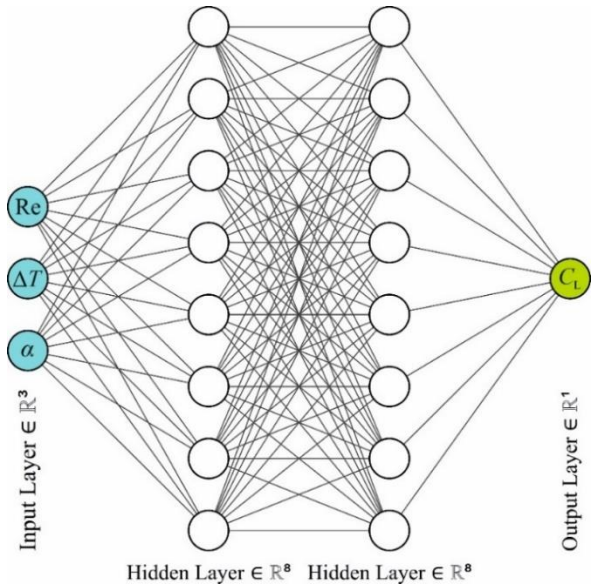

Fig. 3 Schematic representation of the fully convolutional neural network (FCNN) used in this study

The inputs, Reynolds number (Re), temperature difference between upper and lower airfoil surfaces (ΔT), and angle of attack (α), are fed into the network to predict the lift coefficient (CL). In MLP neural networks, the number of hidden layers and the number of suitable neurons in each of the hidden layers vary according to the complexity of the problem. The effect of the number of hidden layers and the number of neurons has been investigated. The neural network learning process is performed with MATLAB software. The adaptive moment estimation (ADAM) optimizer with a learning rate of 0.001 has been used to increase the speed and stability of the learning process.

The values of the Reynolds number, the temperature difference of the upper and lower surfaces, and the angle of attack are considered inputs, and the value of the lift coefficient is the output of the neural network. Also, two hidden layers with 64 neurons have been used. For Reynolds numbers 3.3e4 and 1.7e6, temperature difference from 0 to 200 °C, angle of attack from 0 to 14, and the number of 335 samples have been randomly selected by the Latin Hyperbolic Sampling (LHS) method, and the results of the numerical solution of these samples have been used in the neural network.

The total number of data points obtained from the numerical solution is 335, of which 70% (equivalent to 234) were used for training and 30% (equivalent to 101) was used for testing. To increase the accuracy of the network and the stability of the neural network, all the data are scaled by the largest available values. Also, the input values have been normalized with standard scores (z-scores). To check the accuracy of the neural network, mean squared error (MSE), mean absolute error (MAE), and correlation coefficient (R) parameters have been checked. The relationships related to MSE, MAE, and R are given below, where N is the total number of data, $\hat{y}_i$ is the measured value (measured) of i_{th} data, y_i is the predicted value (predicted) of i_{th} data, and $\hat{\mu}$, μ, $\hat{\sigma}$ and σ are the mean and standard deviation values for (measured) and (predicted) data (Eq. (20), (21) and (22)).

$$MSE = \sum_{i=1}^{N} \frac{(\hat{y}_i - y_i)^2}{N} \tag{20}$$

$$MAE = \sum_{i=1}^{N} \frac{|\hat{y}_i - y_i|}{N} \tag{21}$$

$$R = \frac{1}{N-1} \sum_{i=1}^{N} \left(\frac{\hat{y}_i - \hat{\mu}}{\hat{\sigma}} \right) \left(\frac{y_i - \mu}{\sigma} \right) \tag{22}$$

3. RESULTS AND DISCUSSIONS

3.1 Model Verification

The approach is first used to explore a range of basic airfoils without any surface heating or cooling at low Reynolds numbers. Cl and Cd projections match the results from the literature ideally in these conditions

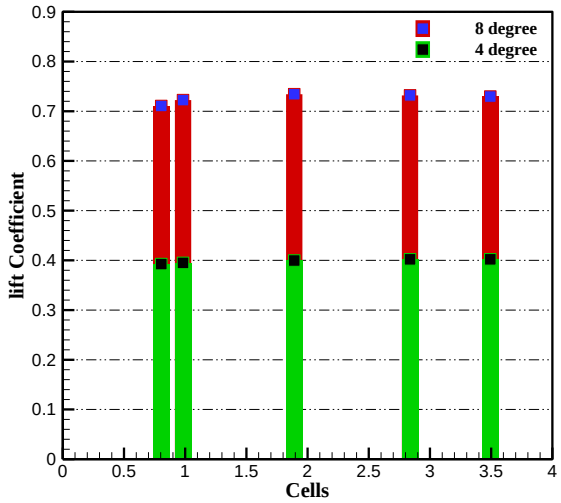

Fig. 4 Grid check for the lift coefficient of a NACA 0012 airfoil in free stream flow with a Mach number of 0.0725, 300 K temperatures, 1 atm pressure, 3.3×104 Reynolds number, and different angles of attack

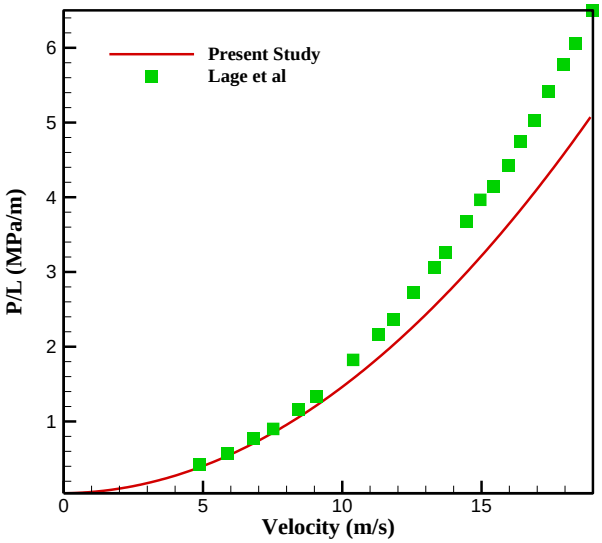

Fig. 6 Simulation results for pressure gradient compared to experimental and theoretical results

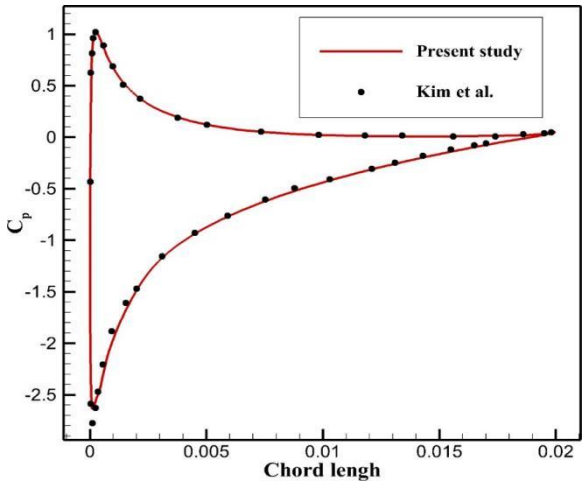

Fig. 5 The pressure coefficient vs. chord length for the NACA 0012 section in a fluid flow with a Mach 0.0725, a temperature of 300 K, pressure of 1 atm, and Reynolds number of 3.3 × 104 at an angle of attack of 8 degrees, comparison of the current results with the data of Kim et al. (Kim et al., 2003)

(Burns & Muller, 1982; Mueller & B. Jansen, 1982; O'Meara & Mueller, 1987). Simulations with several mesh refinement levels are performed for numerical validation. Variations in temperature normal to the wing's surface are much more significant than those perpendicular to the airfoil. As a result, cells far from the surface have larger aspect ratios.

Mesh convergence tests are carried out on a NACA 0012 blade with lower and upper surface temperatures of 260 K and 340 K (ΔT = 40 K) and a homogeneous air flow with a Mach number of 0.0725, pressure of 1 atm, and temperature of 300 K. The Reynolds number of the flow is 3.3×104. Figure 4 illustrates the results of computations with various meshes. The velocity profile as a function of the angle of attack is depicted in Fig. 4. Using a coarse mesh underestimates the lift coefficient (8100 cells). However, no detectable change in the solution is apparent at all angles of attack with finer meshes of 100×50 (35,000 cells) and higher (Fig. 4). The findings with 8100 cells reveal that the velocity profile is overestimated. The pressure distributions are almost identical to 35000 cells or higher. According to Fig. 4, a mesh number of 35,000 is adequate for a converged (mesh-independent) flow solution. This mesh number is utilized in all of the following flow simulations: The highly pressurized zone encompasses the stagnation point. It reduces the airflow velocity along the nose's lower part, causing the nose's upper part to accelerate and produce suction. As a consequence, drag force decreases and airfoil lift force increases. Because of the comparably quasi-steady Re and its further reduced value modified Reynolds number in the nose area, this effect significantly affects the airfoil compact size and nose.

Figure 5 depicts the pressure coefficient solutions along the airfoil surface and compares them with the data of (Kim et al., 2003) to observe a cooperative agreement between the present and literature data. Validation of porous media was done based on (Lage et al., 1997) experimental work, which assessed the pressure gradient of airflow through porous media (Fig. 6). Porous media are homogeneous and isotropic. Thus, the permeability is $11.36 \times 10^{-10} m^2$, the porosity is 0.64, and the inertia coefficient is 0.371, respectively.

3.2 Effect of Temperature On Airfoil

In Fig. 7 (a), we compare different airfoil cases based on temperature. It can be observed that the airfoil increases as the temperature difference between the upper and lower surfaces is delayed. Also, in this figure, we compared two different Reynolds numbers: Reynolds 3.3×10^4, where the chord length is 0.2 m, and Reynolds 1.7×10^6, where the chord length is 1 m, respectively. Figure 7 (a) displays the lift coefficient as a function of the angle of attack for full-scale and micro-scale airfoils. At a 12° angle of attack,

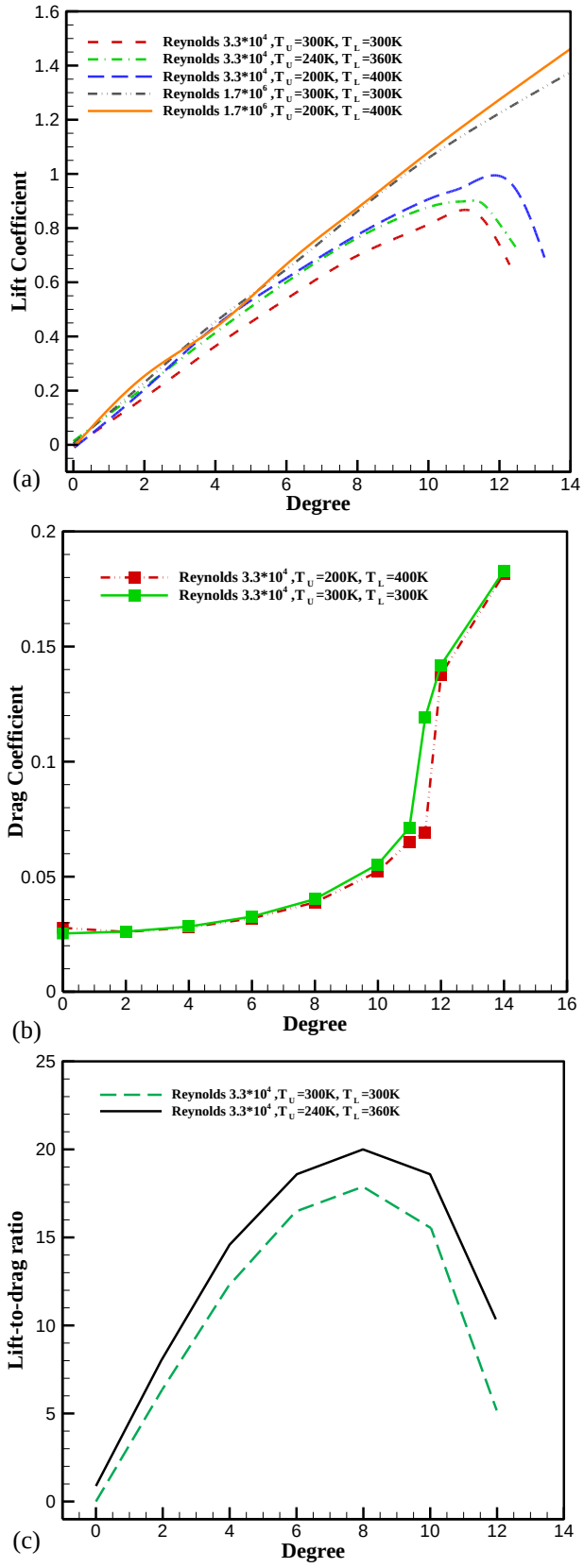

Fig. 7 The lift coefficient (a), drag coefficient (b), and lift-to-drag ratio (c) variations versus angle of attack for a NACA 0012 airfoil at 300 K with a Mach number of 0

the micro-scale airfoil is expected to have a substantially higher increase in lift coefficient. Due to the upper

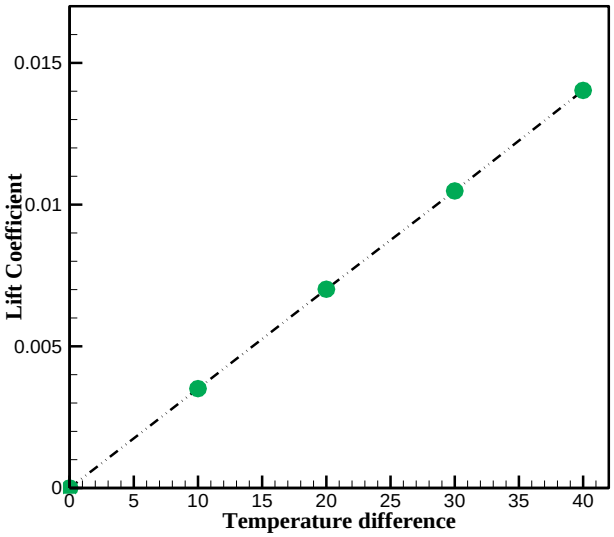

Fig. 8 NACA 0012 airfoil lift coefficient variation, simulation analysis, Mach number of 0.0725, Reynolds number of 3.3×104, at 0° angle of attack

surface's low temperature, flow separation is reduced, and stall is postponed to a higher angle of attack (from approximately 11° to nearly 12°). However, no discernible improvement in lift force response is expected for the full-scale airfoil. Figure 7 (b) contrasts the findings of the drag coefficient variation in Reynolds number Re = 3.3 × 10^4, T_U = 200 K, T_L = 400 K.

Only in the micro-scale airfoil does the drag force coefficient dramatically reduce. The drag decrease rate is more pronounced than the lift coefficient increase rate and the transverse stall angle. Figure 7 (c) shows a similar trend for the sectional L/D ratio for Reynolds number =3.3 × 10^4, T_U = 200 K, T_L = 400 K and Reynolds number = 3.3 × 10^4, T_U = 300 K, T_L = 300 K. At a total angle of attack of 12°, the micro-scale airfoil L/D increases from 1 to 20.

Figure 8 shows the lift coefficient at the zero angle of attack for different temperature differences. On the upper surface of the airfoil, the temperature is less than 300 K, and on the lower surface of the airfoil, the temperature is higher than 300 K. Due to the interchange of thermal and kinetic energy in the flow zone outside of the velocity boundary layer, the flow is accelerated in comparison to the baseline.

In comparison to the baseline, the flow in this area moves at a substantially faster axial velocity. This indicates that the upper cooler surface has a lower pressure at the velocity boundary layer's edge than in the base case, which is also the airfoil surface pressure at this point (Fahland et al., 2021; Chen et al., 2022). This differential pressure is what causes the increased lift to be produced. The delay of flow separation at greater angles of attack also occurs from the acceleration of the flow on the upper surface.

Figure 9 shows the temperature, pressure, and velocity contours for two cases with a temperature difference between the upper and lower of the airfoil surface and lower airfoil surfaces and without a temperature difference between the airfoil surfaces. When

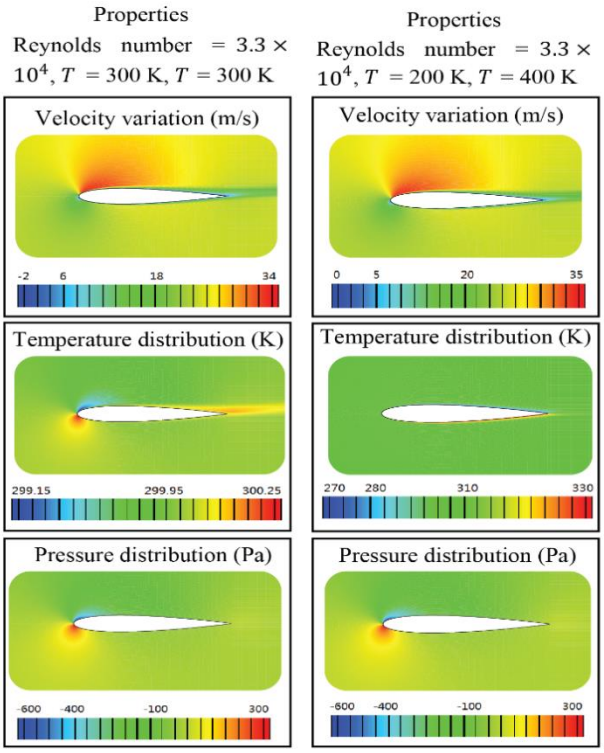

Fig. 9 Velocity, temperature, and pressure contour for two cases with and without temperature differences on the airfoil surface

compared to the heated airfoil, Fig. 9 (Pressure Distribution) shows that the cooled airfoil has significantly increased pressure, leading to increased lift. The relevant velocity profiles are shown in Fig. 9 (Velocity Variation). The heated airfoil has significant flow separation near the leading edge and is mostly in stalled flow. However, the cooled airfoil obviously exhibits far less separation, which results in more lift and a lower airfoil drag penalty.

Figure 10 depicts the thermal and velocity barrier layers on the upper (240 K) and lower (400 K) sides of the microscale airfoil at a 10% chordwise station. For comparison, the original condition (including both edges at 300 K) is also illustrated. The flow is accelerated in reference to the baseline due to the transmission of thermal and angular velocity on the top surface of the airfoil that has been cooled to 240 K as shown in Fig. 10. The opposite behavior is observed on the bottom surface, which has now been heated to 400 K.

The effect of the temperature difference on the Reynolds number is 0.3×104 when we consider the flow to be laminar (Fig. 11). To see the influence of the surface temperature on the drag coefficient, a NACA 0012 airfoil at Reynolds 3000 with the angle of attack $\alpha = 0$, and the surface temperature changing within the range of 200–300 K is considered. Results show that C_D increases by 6.8% when the surface temperature changes from 200 K to 300 K (Fig. 11).

The pressure drag and the viscous drag are two crucial components that make up the drag force. Since the drag force for a symmetric airfoil at zero angle of attack

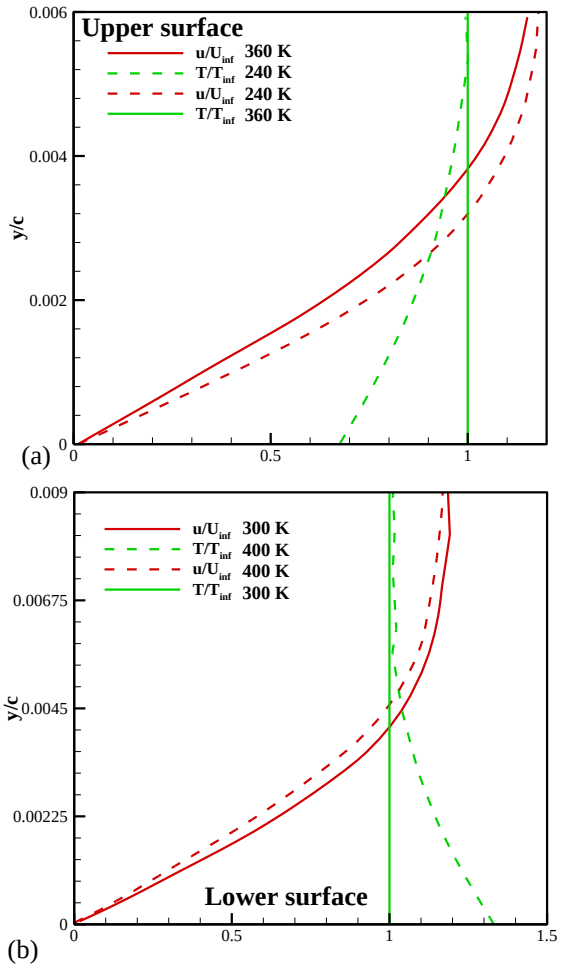

Fig. 10 Thermal and velocity boundary (a) upper (240 K) and (b) lower (400 K) layers at the 0° angle of attack station of the NACA 0012 section, which is in freestream and has a Mach number of 0.0725, a temperature of 300 K, a pressure of 1 atm, and a Reynolds number of 3.3×10^4

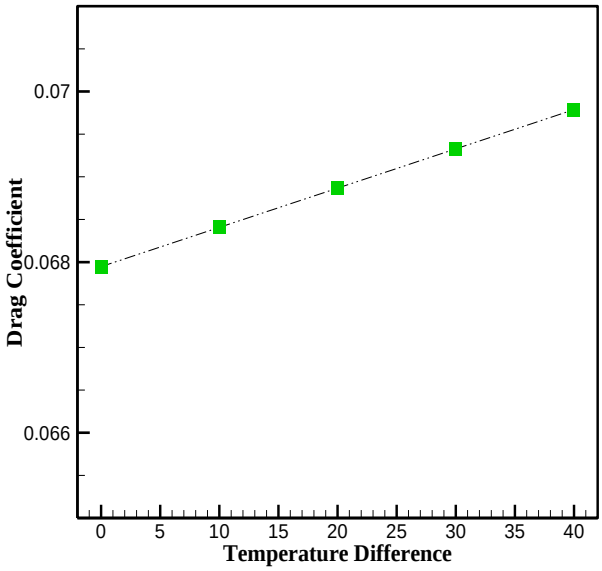

Fig. 11 NACA 0012 airfoil drag coefficient change, simulation analysis, Mach number 0.0034, Reynolds number 0.3×10^4, at 0° angle of attack

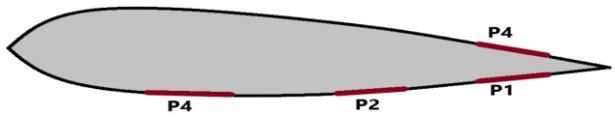

Fig. 12 Porous media location on airfoil

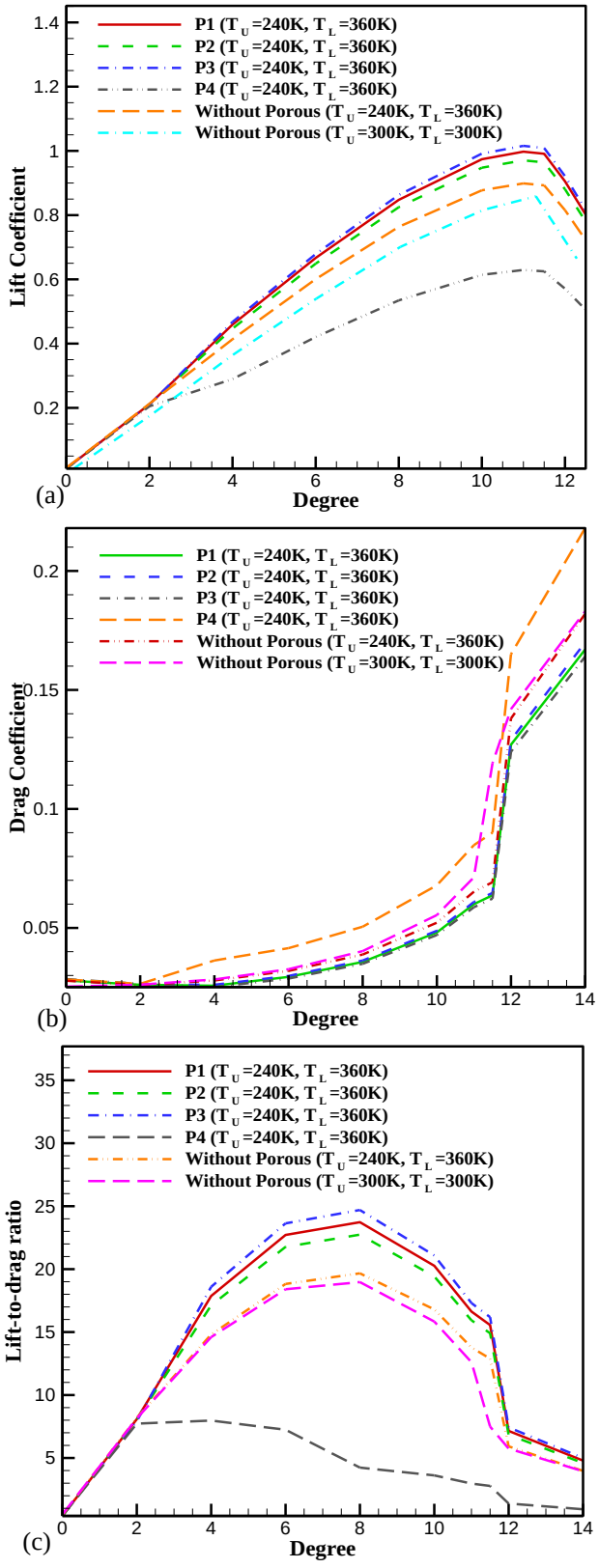

Fig. 13 shows the lift coefficient (a), drag coefficient (b) and lift-to-drag ratio, (c) variations versus angle of attack for a NACA 0012 airfoil at 300 K, Mach number of 0.0725, and pressure of 1 atm

primarily results from momentum loss in the viscous boundary layer, its increase with rising surface temperature is explicable in terms of the altered fluid characteristics in this layer. It is evident that when the temperature increases, the drag coefficient and shear stress also increase. In Fig. 11, when the temperature is raised from 260 K to 380 K, the dynamic viscosity rises by over 24%. High fluid velocities (Mach higher than 0.3), as well as a change in the fluid's temperature, density, and pressure due to heating, can produce compressibility effects. Because of the extremely low Mach number, there are no compressibility effects brought on by fast fluid velocities. As a result, it is presumed that the heating has little to no impact on the normal gradient velocity $\partial u/\partial n$ on the wall. However, the heating's effects on compressibility necessitate using a compressible solution to mimic the correct behavior.

3.3 Effect of Temperature and Porous Media on Airfoil

Porous media have different results on the airfoil based on location. Porous media on the leading edge and trailing edge are hard to build. For this reason, a narrow strip has been considered porous to minimize its structural problems. In Fig. 12, we chose four different places to choose the most optimal mode. P1, P2, P3, and P4 are at a distance of 0.25c, 0.5c, 0.75c, and 0.25c from the trailing edge, respectively.

We placed porous media in different parts of the airfoil and checked the effect of temperature on its lift, drag coefficients, and lift-to-drag, as shown in Fig. 13.

As can be seen, most of the porous media cause the stall angle of attack to increase. In Fig. 13, the lift coefficient, it can be seen that P1, P2, and P3 have good performance and have increased the lift coefficient, but P4 has a weaker performance compared to the state without press. It is observed that the effect of temperature and porous media on the airfoil compared to the mode without temperature and porous media has very good performance and has a higher lift coefficient and a lower drag coefficient. Also, as a result, it can be seen that most of the porous media have more lift-to-drag than normal airfoils.

3.4 Effect of Temperature and Porous Media on Airfoil

In order to find the best and most optimal network architecture, the effect of the number of layers and neurons on the MSE, MAE, and R is given in Table A1 (Appendix) and Fig. 14. It can be seen that the best network architecture belongs to three hidden layers with 15, 20, and 20 neurons, respectively. The number of weights in this network is not very high, and on the other hand, its value of MSE is less than the other investigated architectures.

Table A2 and Fig. 15 also show the effect of the number of epochs. It can be seen that the time required to learn the network increases almost linearly with the increase in the number of epochs, but the amount of MSE in epochs below 2000 is noticeably reduced, and for epochs higher than 2000, it does not lead to significant improvement. Therefore, choosing an epoch value greater

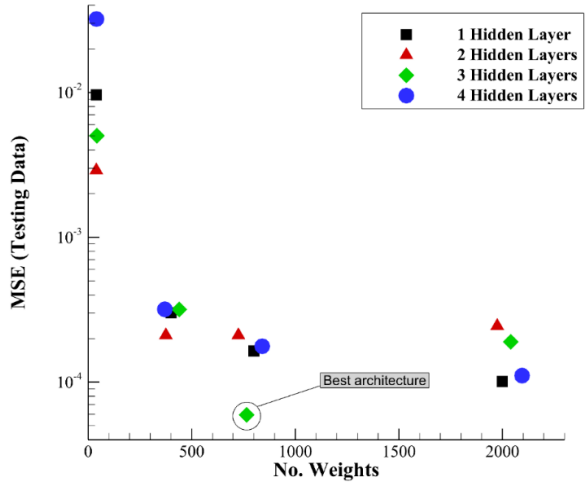

Fig. 14 The effect of the number of hidden layers and the number of neurons on MSE (Testing Data)

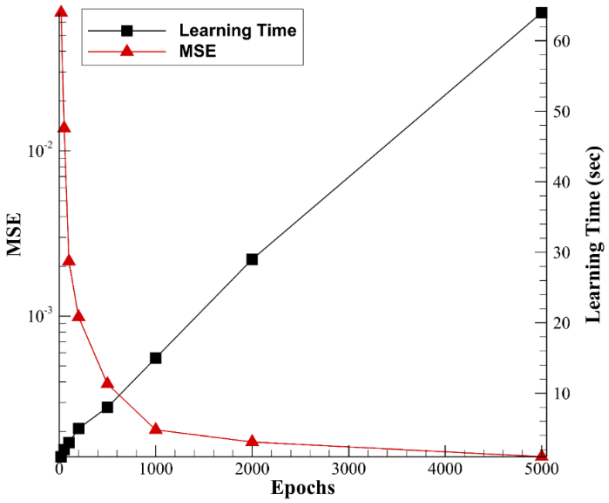

Fig. 15 The effect of the number of epochs on MSE

than 2000 only increases the computational time and cost without any improvement in the accuracy of the network.

To check the obtained results, regression charts are given in Fig. 16 (a) and (b). It is observed that despite the value of R being very close to 1, which indicates a regression with high accuracy, the data distribution is not balanced, and a large number of them are related to drag coefficients close to zero. On the other hand, according to Fig. 16 (c), for the 200-degree temperature difference, the accuracy in the area shown is not suitable, which is the stall area. In contrast, in CL areas close to zero, a very accurate prediction has been made. On the other hand, according to the nature of the problem, the area of concern and criticality is around the stall.

Several methods have been proposed to overcome such problems in machine learning. Among the most important of them are cost-sensitive learning (Sutherland, 1893; Bergman et al., 2011) and the synthetic minority over-sampling technique for regression applications (SMOTER) (O'Meara & Mueller, 1987). For cost-sensitive learning methods to be efficient, it is necessary that the rare data of interest can be separated by a function of the output (the lift coefficient in the present problem).

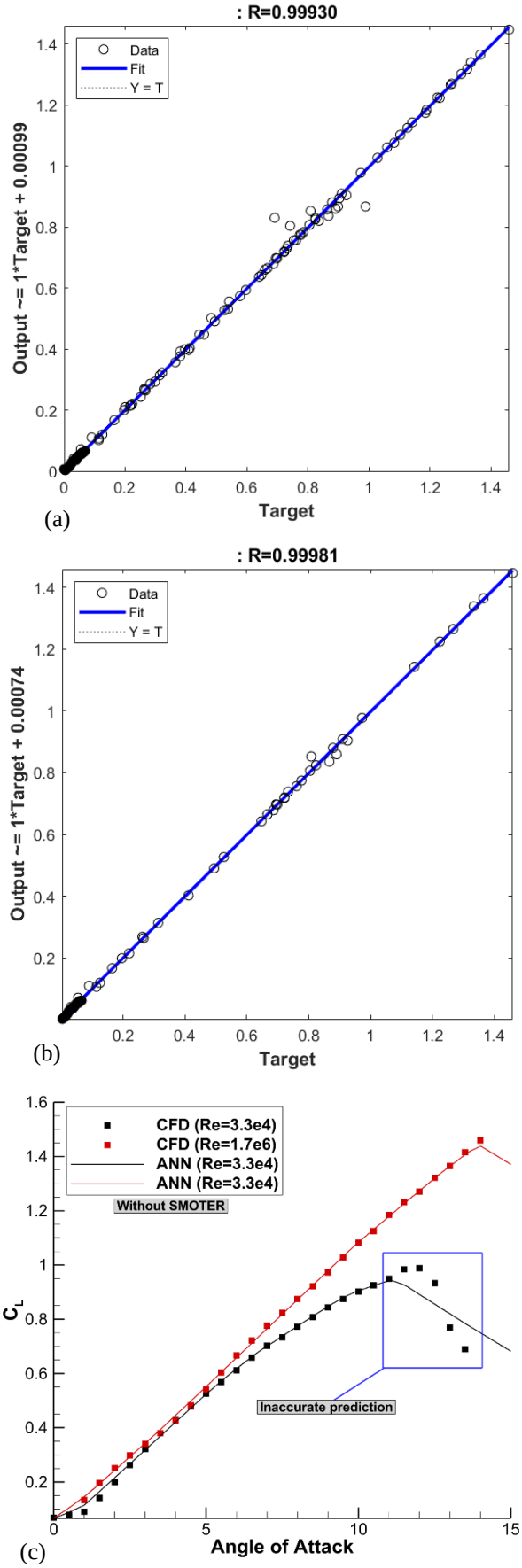

Fig. 16 (a) shows the Regression plot for CL (Training Data), (b) Regression plot for CL (Testing Data) and (c) Lift coefficient – Angle of Attack (Without SMOTER)

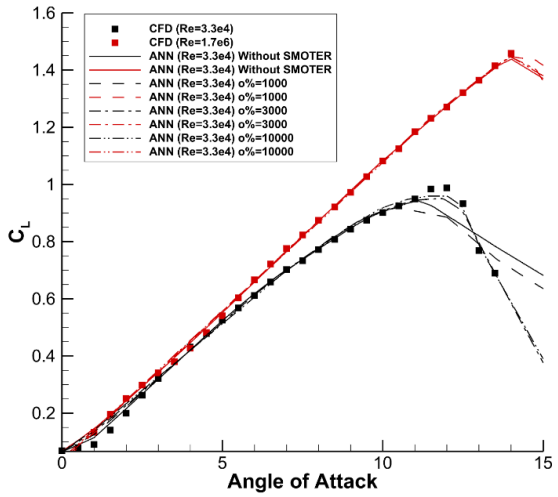

Fig. 17 Lift coefficient – Angle of Attack (with SMOTER)

At the same time, this is not possible in this research with the available data. Therefore, the second method, SMOTER, has been used. In this method, in general, frequent data is reduced (under-sampling) and rare data is added (over-sampling). Adding synthetic data is done with the help of K-nearest neighbors (K-NN) and interpolation. A description of the algorithm is available in (O'Meara & Mueller, 1987).

For the implementation of SMOTER, the data related to the stall areas, which are limited to 7 numbers, has been selected as rare data and the rest as frequent data. To check the effect of oversampling value and K value on K-NN, MSE, MAE, and R values for training and testing data are given in Table A3. It can be seen that the best results are related to K=3, and an oversampling of 1000%.

Also, in Fig. 17, the graphs of the changes in the lift coefficient concerning the angle of attack are given. It can be seen that increasing the amount of oversampling increases the accuracy in the desired area. But raising it too much will cause problems like overfitting, so by estimating the results and considering the importance of accurately predicting the stall area, it is appropriate to choose oversampling = 3000%. Also, K = 3 has been used in the K-NN algorithm to generalize the newly generated synthetic data. Another noteworthy point is that despite the fact that the stall region for Re = 1.7×10^6 was not used for the learning process of the neural network, the network has an accurate prediction of this region, which starts at about 14 degrees. CFD results separately confirm this value.

4. CONCLUSION

According to the current models, although changing the surface temperature has little influence at full scale due to the thinness of the thermal and velocity boundary layers compared to the airfoil chord, it has a substantial impact on lift coefficient. The heat transfer in the considerably smaller nose area of the small-scale airfoil really accounts for the majority of the effect. By directly using heat transfer, which dominates microscale systems, we show how to improve lift, lower drag, and expand the operational envelope of airfoils. And we get these results from the neural network:

- The MLP neural networks have been developed to accurately predict the lift coefficient.
- The SMOTER algorithm was applied to increase the accuracy of the network in the area with very little data but of interest. This algorithm helps to predict the stall area with much more accuracy.
- The developed neural network can be used to predict the stall region at different Reynolds numbers and different temperature differences.

The significant findings of our study reveal that the lift-to-drag coefficient can be enhanced by raising the temperature. Moreover, the utilization of the porous state and temperature differential further contributes to an increase in the lift-to-drag coefficient. Additionally, we successfully employed a neural network to accurately predict the outcome when altering the temperature, particularly when dealing with a higher number of cases.

CONFLICT OF INTEREST

The author declares that there is no conflict of financial or non-financial interest to disclose.

AUTHORS CONTRIBUTION

Conceptualization, **A. Wadi Al-Fatlawi,** methodology, **J. Hashemi, A. Wadi Al-Fatlawi**; analysis, **Hashemi, A. Wadi Al-Fatlawi**; investigation, **J. Hashemi, A. Wadi Al-Fatlawi**, **S. Hossain**; writing—original draft preparation, **J. Hashemi, A. Wadi Al-Fatlawi, S. Hossain**; writing—review and editing, **J. Hashemi, A. Wadi Al-Fatlawi**, **S. Hossain,** and **M. El Haj Assad**. All authors have read and agreed to the published version of the manuscript.

REFERENCES

Ahmed, S., Kamal, K., Ratlamwala, T. A. H., Mathavan, S., Hussain, G., Alkahtani, M., & Alsultan, M. B. M. (2022). Aerodynamic analyses of airfoils using machine learning as an alternative to RANS simulation. *Applied Sciences*, *12*(10), 5194. https://www.mdpi.com/2076-3417/12/10/5194

Bekka, N., Bessaïh, R., Sellam, M., & Chpoun, A. (2009). Numerical study of heat transfer around the small scale airfoil using various turbulence models, numer. *Numerical Heat Transfer, Part A: Applications*, *56*, 946–969. https://doi.org/https://doi.org/10.1080/10407780903508005

Bergman, T. L., Lavine, A. S., Incropera, F. P., & DeWitt, D. P. (2011). *Introduction to heat transfer*. John Wiley & Sons.

Bhatnagar, S., Afshar, Y., Pan, S., Duraisamy, K., & Kaushik, S. (2019). Prediction of aerodynamic flow fields using convolutional neural networks. *Computational Mechanics*, *64*(2), 525-545. https://doi.org/10.1007/s00466-019-01740-0

Burns, T., & Muller, T. (1982). *Experimental studies of the eppler 61 airfoil at low reynolds numbers*. 20th Aerospace Sciences Meeting. https://doi.org/10.2514/6.1982-345

Chen, Z., Shi, Z., Chen, S., & Yao, Z. (2022). Stall flutter suppression of NACA 0012 airfoil based on steady blowing. *Journal of Fluids and Structures*, *109*, 103472. https://doi.org/https://doi.org/10.1016/j.jfluidstructs.2021.103472

Crivellini, A., & D'Alessandro, V. (2014). Spalart–allmaras model apparent transition and rans simulations of laminar separation bubbles on airfoils. *International Journal of Heat and Fluid Flow*, *47*, 70-83. https://doi.org/https://doi.org/10.1016/j.ijheatfluidflow.2014.03.002

Ethiraj, L., & Pillai, S. N. (2021). Effect of trailing-edge modification over aerodynamic characteristics of NACA 0020 airfoil. *Wind and Structures*, *33*(6), 463-470. https://doi.org/10.12989/was.2021.33.6.463

Eucken, A. (1940). Allgemeine gesetzmäßigkeiten für das wärmeleitvermögen verschiedener stoffarten und aggregatzustände. *Forschung auf dem Gebiet des Ingenieurwesens A*, *11*(1), 6-20. https://doi.org/10.1007/BF02584103

Fahland, G., Stroh, A., Frohnapfel, B., Atzori, M., Vinuesa, R., Schlatter, P., & Gatti, D. (2021). Investigation of blowing and suction for turbulent flow control on airfoils. *59*(11), 4422-4436. https://doi.org/10.2514/1.J060211

Ferziger, J. H., Perić, M., & Street, R. L. (2002). Computational methods for fluid dynamics. *Berlin: springer*, *3*, 196-200. https://doi.org/10.1007/978-3-319-99693-6

Grasmeyer, J., & Keennon, M. (2001). *Development of the black widow micro air vehicle*. 39th Aerospace Sciences Meeting and Exhibit. https://doi.org/10.2514/6.2001-127

Hinz, D. F., Alighanbari, H., & Breitsamter, C. (2013). Influence of heat transfer on the aerodynamic performance of a plunging and pitching NACA0012 airfoil at low Reynolds numbers. *Journal of Fluids and Structures*, *37*, 88-99. https://doi.org/https://doi.org/10.1016/j.jfluidstructs.2012.08.012

Jordaan, H., Stephan Heyns, P., & Hoseinzadeh, S. (2021). Numerical development of a coupled one-dimensional/three-dimensional computational fluid dynamics method for thermal analysis with flow maldistribution. *Journal of Thermal Science and Engineering Applications*, *13*(4). https://doi.org/10.1115/1.4049040

Kim, J., Rusak, Z., & Koratkar, N. (2003). Small-Scale Airfoil aerodynamic efficiency improvement by surface temperature and heat transfer. *Aerospace Research Central*, *41*(11), 2105-2113. https://doi.org/10.2514/2.6829

Lage, J. L., Antohe, B. V., & Nield, D. A. (1997). Two types of nonlinear pressure-drop versus flow-rate relation observed for saturated porous media. *Journal of Fluids Engineering*, *119*(3), 700-706. https://doi.org/10.1115/1.2819301 %J Journal of Fluids Engineering

Landrum, D., & Macha, J. (1987). *Influence of a heated leading edge on boundary layer growth, stability, and transition.* 19th AIAA, Fluid Dynamics, Plasma Dynamics, and Lasers Conference. https://doi.org/10.2514/6.1987-1259

Li, X. K., Liu, W., Zhang, T. J., Wang, P. M., & Wang, X. D. (2019). Analysis of the effect of vortex generator spacing on boundary layer flow separation control. *Applied Sciences*, *9*(24), 5495. https://www.mdpi.com/2076-3417/9/24/5495

Liepmann, H. W., & Fila, G. H. (1947). *Investigations of effects of surface temperature and single roughness elements on boundary-layer transition* (No. NACA-TR-890). https://ntrs.nasa.gov/api/citations/19930091958/downloads/19930091958.pdf

Liu, Y., Zhu, Y., Li, D., Huang, Z., & Bi, C. (2023). Computational simulation of mass transfer in membranes using hybrid machine learning models and computational fluid dynamics. *Case Studies in Thermal Engineering*, *47*, 103086. https://doi.org/https://doi.org/10.1016/j.csite.2023.103086

Llorente, E., & Ragni, D. (2020). Trailing-edge serrations effect on the performance of a wind turbine. *Renewable Energy*, *147*, 437-446. https://doi.org/https://doi.org/10.1016/j.renene.2019.08.128

Mabey, D. G. (1990). Effects of heat transfer on aerodynamics and possible implications for wind tunnel tests. *Progress in Aerospace Sciences*, *27*(4), 267-303. https://doi.org/https://doi.org/10.1016/0376-0421(90)90001-Z

Mueller, T. J., & B. Jansen, J. (1982). *Aerodynamic measurements at low reynolds numbers*. 12th Aerodynamic Testing Conference. https://doi.org/10.2514/6.1982-598

Norton, D. J., Macha, J. M., & Young, J. C. (1973). Surface *Temperature Effect on Subsonic Stall*. *Aerospace Research Central*, *10*(9), 581-587. https://doi.org/10.2514/3.61929

O'Meara, M. M., & Mueller, T. J. (1987). Laminar separation bubble characteristics on an airfoil at low Reynolds numbers. *Aerospace Research Central*, *25*(8), 1033-1041. https://doi.org/10.2514/3.9739

Oosedo, A., Abiko, S., Konno, A., & Uchiyama, M. (2017). Optimal transition from hovering to level-flight of a quadrotor tail-sitter UAV. *Autonomous Robots*, *41*(5), 1143-1159. https://doi.org/10.1007/s10514-016-9599-4

Raghunathan, S., & Mitchell, D. (1995). Computed effects of heat transfer on the transonic flow over an aerofoil. *Aerospace Research Central*, *33*(11), 2120-2127. https://doi.org/10.2514/3.12956

Samiee, A., Djavareshkian, M. H., Feshalami, B. F., & Esmaeilifar, E. (2018). Improvement of airfoils aerodynamic efficiency by thermal camber phenomenon at low reynolds number. *Journal of Aerospace Technology and Management*, *10*. https://doi.org/10.5028/jatm.v10.954

Selimefendigil, F., & Öztop, H. F. (2021). Thermoelectric generation in bifurcating channels and efficient modeling by using hybrid CFD and artificial neural networks. *Renewable Energy*, *172*, 582-598. https://doi.org/https://doi.org/10.1016/j.renene.2021.03.046

Seyhan, M., Sarioglu, M., & Akansu, Y. E. (2021). Influence of leading-edge tubercle with amplitude modulation on NACA 0015 airfoil. *Aerospace Research Central*, *59*(10), 3965-3978. https://doi.org/10.2514/1.J060180

Silva, D. d., & Malatesta, V. (2020). Numerical simulation of the boundary layer control on the NACA 0015 airfoil through vortex generators. *Journal of Aerospace Technology and Management*, *12*. https://doi.org/10.5028/jatm.v12.1102

Stock, H. W. (2002). Wind tunnel–flight correlation for laminar wings in adiabatic and heating flow conditions. *Aerospace Science and Technology*, *6*(4), 245-257. https://doi.org/https://doi.org/10.1016/S1270-9638(02)01166-5

Sutherland, W. (1893). LII. The viscosity of gases and molecular force. *The London, Edinburgh, and Dublin Philosophical Magazine and Journal of Science*, *36*(223), 507-531. https://doi.org/10.1080/14786449308620508

Wang, L., Alam, M. M., Rehman, S., & Zhou, Y. (2022). Effects of blowing and suction jets on the aerodynamic performance of wind turbine airfoil. *Renewable Energy*, *196*, 52-64. https://doi.org/https://doi.org/10.1016/j.renene.2022.06.126

Yan, Y., Avital, E., Williams, J., & Cui, J. (2019). CFD analysis for the performance of micro-vortex generator on aerofoil and vertical axis turbine. *Journal of Renewable and Sustainable Energy*, *11*(4). https://doi.org/10.1063/1.5110422

Zadorozhna, D. B., Benavides, O., Grajeda, J. S., Ramirez, S. F., & de la Cruz May, L. (2021). A parametric study of the effect of leading edge spherical tubercle amplitudes on the aerodynamic performance of a 2D wind turbine airfoil at low Reynolds numbers using computational fluid dynamics. *Energy Reports*, *7*, 4184-4196. https://doi.org/https://doi.org/10.1016/j.egyr.2021.06.093

APPENDIX

Table A1 The effect of the number of hidden layers and the number of neurons

Input	1st	2nd	3rd	4th	output	No. Weights	Training	Testing	Training	Testing	Training	Testing
3	10	0	0	0	1	40	8.16E-03	9.62E-03	6.58E-02	7.07E-02	0.971487	0.968163
3	100	0	0	0	1	400	4.79E-04	3.01E-04	7.31E-03	7.42E-03	0.998348	0.999048
3	200	0	0	0	1	800	3.23E-04	1.64E-04	5.06E-03	4.75E-03	0.998886	0.999487
3	500	0	0	0	1	2000	2.39E-04	1.01E-04	4.03E-03	3.55E-03	0.999175	0.999679
3	5	4	0	0	1	39	3.76E-03	2.90E-03	3.25E-02	3.11E-02	0.986944	0.990643
3	20	15	0	0	1	375	3.80E-04	2.11E-04	7.06E-03	6.32E-03	0.998689	0.999336
3	25	25	0	0	1	725	3.49E-04	2.11E-04	6.45E-03	6.29E-03	0.998797	0.999324
3	45	40	0	0	1	1975	3.65E-04	2.44E-04	6.40E-03	6.56E-03	0.998742	0.999230
3	3	5	3	0	1	42	4.84E-03	5.03E-03	3.43E-02	3.64E-02	0.983191	0.983867
3	10	20	10	0	1	440	4.94E-04	3.17E-04	8.77E-03	8.59E-03	0.998298	0.999064

3	15	20	20	0	1	765	2.05E-04	5.94E-05	5.04E-03	3.94E-03	0.999297	0.999811
3	30	35	25	0	1	2040	3.89E-04	1.90E-04	6.08E-03	5.79E-03	0.998659	0.999418
3	2	4	4	2	1	40	2.94E-02	3.21E-02	6.97E-02	6.81E-02	0.896686	0.895007
3	5	20	10	5	1	370	4.66E-04	3.18E-04	9.21E-03	8.70E-03	0.998394	0.998974
3	10	20	20	10	1	840	3.25E-04	1.77E-04	6.82E-03	6.77E-03	0.998881	0.999478
3	25	30	25	20	1	2095	2.57E-04	1.11E-04	4.91E-03	4.56E-03	0.999117	0.999645

Table A2 The effect of the number of Epochs

Epoch	Training Time (sec)	MSE		MAE		R	
		Training	Testing	Training	Testing	Training	Testing
20	1.00	6.86E-02	7.92E-02	1.85E-01	1.94E-01	0.852320	0.826788
50	2.00	1.37E-02	1.48E-02	8.37E-02	8.64E-02	0.953834	0.950702
100	3.00	2.14E-03	1.32E-03	2.61E-02	2.42E-02	0.992662	0.995806
200	5.00	9.88E-04	6.33E-04	1.60E-02	1.62E-02	0.996600	0.998009
500	8.00	3.88E-04	1.96E-04	7.39E-03	6.67E-03	0.998666	0.999376
1000	15.00	2.05E-04	5.94E-05	5.04E-03	3.94E-03	0.999297	0.999811
2000	29.00	1.73E-04	5.42E-05	4.54E-03	4.01E-03	0.999407	0.999831
5000	64.00	1.41E-04	4.36E-05	3.62E-03	2.91E-03	0.999516	0.999867

Table A3 The effect of SMOTER on the system accuracy

Dataset	MSE		MAE		R	
	Train	Test	Train	Test	Train	Test
Original Data (335) (7 Rare)	2.05E-04	5.94E-05	5.04E-03	3.94E-03	0.999297	0.999811
SMOTER (405) (77 Rare) K=3 o=1000%	3.45E-04	3.14E-04	8.20E-03	8.05E-03	0.998895	0.998960
SMOTER (405) (77 Rare) K=5 o=1000%	4.53E-04	5.14E-04	9.00E-03	8.51E-03	0.998558	0.998298
SMOTER (405) (77 Rare) K=7 o=1000%	3.81E-04	3.02E-04	9.11E-03	8.09E-03	0.998782	0.998998
SMOTER (545) (217 Rare) K=3o=3000%	5.06E-04	4.79E-04	1.32E-02	1.27E-02	0.998381	0.998433
SMOTER (685) (357 Rare) K=3 o=5000%	9.98E-01	6.43E-04	1.65E-02	1.60E-02	0.997594	0.997774